Journal of Materials Chemistry A

ROYAL SOCIETY OF CHEMISTRY

PAPER

View Article Online
View Journal | View Issue

Cite this: J. Mater. Chem. A, 2023, 11, 5337

Synthesis, properties and catalytic performance of the novel, pseudo-spinel, multicomponent transition-metal selenides†

Andrzej Mikuła, *[a] Juliusz Dąbrowa, [a] Maciej Kubowicz, [a] Jakub Cieślak,[b] Wiktor Lach,[a] Miłosz Kożusznik,[a] Mathias Smialkowski[c] and Ulf-Peter Apfel [cd]

Received 2nd December 2022
Accepted 14th February 2023

DOI: 10.1039/d2ta09401k

rsc.li/materials-a

With electrocatalysis being the very foundation of multiple energy conversion technologies, the search for more effective, and affordable catalysts is becoming increasingly important for their further development. Recently, the multicomponent approach, together with the electronic structure calculations, have established themselves as promising ways of designing such materials. In the presented study, both these approaches are combined, leading to the development of a unprecedented $(Co,Fe,Ni)_3Se_4$ chalcogenide catalyst. Based on the extensive density functional theory calculations (DFT), and structural data, the impact of the multi-element atomic arrangement is discussed, and the possible benefits of such a design strategy are identified. The transport and catalytic properties of the materials are studied, showing excellent charge transfer capabilities, combined with very high catalytic activity with regard to the hydrogen evolution reaction (HER), as evidenced by the current densities of 120, 500, and 1000 mA cm^{-2} at overpotentials of 250, 360, and 450 mV. Of importance, all these results are achieved for the bulk-type electrode, obtained by a simple and scalable process, a considerable advantage over most of the state-of-the-art electrocatalysts, requiring costly and time-consuming nano-structuring of the electrode layer.

Introduction

The era of the climate crisis, combined with the ever-growing worldwide energy demand, imposes the development of new ways of energy conversion that will allow for replacing fossil fuel-based technologies in the foreseeable future. One of the groups with particularly high potential regarding a wide variety of possible applications in this area, are transition-metal chalcogenides (TMCh), with their outstanding versatility being a direct consequence of their unique structural, electrical, and transport properties. Historically, TMCh were associated mainly with thermoelectric applications and are still considered to be the benchmark for other materials, displaying performance beyond the capabilities of other materials groups.[1–10] However, recently, they have gained a lot of interest with regard to the possibility of their utilization in a number of other technologies operating on the basis of electrocatalytic processes, including photochemistry,[11–13] sensors,[12,14,15] fuel cells, and catalysis.[12,16,17] This interest stems from their excellent catalytic activity with respect to some of the most fundamental catalytic reactions, namely hydrogen evolution reaction (HER), and the oxygen evolution reaction (OER). This is evidenced by the low overpotentials reached at current densities of 10 mA cm^{-2} at approximately 60–200 and 200–300 mV, towards HER[18] and OER[19,20] respectively, recorded for various TMCh compounds. Currently, the most popular group of chalcogenides in this regard, are transition-metal disulfides $TMCh_2$,[16,18,21–25] due to their fast-charge transfer abilities (at the level of 10^{-3}–10^{-4} cm s^{-1} for TM dichalcogenides[26]), presence of disulfide linkages, as well as the presence of edge and surface defect sites. One of the most prominent examples here is molybdenum disulfide, exhibiting excellent electrochemical activity towards hydrogen evolution reaction (HER) in both acidic and alkaline media.[23–25] Also, cobalt- and iron-rich $TMCh_2$ compositions are noted for their high activity towards both HER and OER.[24,27] However, despite the popularity and satisfactory performance of $TMCh_2$ compounds, other directions of studies are also constantly pursued.

An important breakthrough in this context was the development of pentlandite-structured, TM_9Ch_8 electrocatalysts, proposed back in 2016 by Konkena *et al.*[28] Structural properties and the electronic structure of pentlandites indicate extremely

[a]AGH University of Science and Technology, Faculty of Materials Science and Ceramics, al. Mickiewicza 30, 30-059 Krakow, Poland. E-mail: amikula@agh.edu.pl
[b]AGH University of Science and Technology, Faculty of Physics and Applied Computer Science, al. Mickiewicza 30, 30-059 Krakow, Poland
[c]Ruhr-Universität Bochum, Fakultät für Chemie und Biochemie, Anorganische Chemie I, Universitätsstrasse 150, 44801 Bochum, Germany
[d]Fraunhofer UMSICHT, Department for Electrosynthesis, Osterfelder Str. 3, 46047 Oberhausen, Germany

† Electronic supplementary information (ESI) available. See DOI: https://doi.org/10.1039/d2ta09401k

efficient mechanisms of hydrogen adsorption at chalcogenide vacancy sites, together with increased thermodynamic stability. At the same time, strong overlapping of the states nearby bandgap area promotes high charge carrier concentration, fast charge-transfer abilities and overall good electrical performance.[28–33] In fact, Konkena *et al.*[28] reported an excellent HER performance of $Fe_{4.5}Ni_{4.5}S_8$, comparable to the best HER metallic catalysts, with an overpotential of 280 mV and Tafel slope of 72 mV dec^{-1}. The same team also showed that by tailoring the Fe–Ni ratio in pentlandite, a very good OER performance with an overpotential at 354 mV and Tafel slope at 56 mV dec^{-1} can also be also achieved,[34] providing an extremely interesting possibility of producing affordable, bifunctional catalysts. What is worth noting is the fact that most of these results were obtained for bulk, rock-like geometries, an unprecedented feature with potentially huge upside, as it enables utilizing very simple and cheap methods of electrode production.

Another group of TMCh exhibiting similar structural features to pentlandites, yet much less studied, are dense-packed, Se-based, monoclinic *C*2/*m*-structured pseudo-spinels, characterized by the presence of only octahedral cationic sites. Similarly, as in pentlandites, the very close, intermetallic interactions between cations, together with a clear tendency for creation of Ch vacancies, have the potential for providing a high concentration of active sites,[31,35–37] making them highly promising bifunctional catalysts. For instance, extremely high current densities of 400 mA cm^{-2} at an overpotential of 320 mV dec^{-1} (OER) were reported for monometallic Co_3Se_4 anchored to cobalt foam.[38] By expanding TM_3Se_4 into multicomponent areas of phase diagrams, further enhancement of electrochemical activity appears to be possible, as presented for $Fe_xCo_{3-x}Se_4$ or Ni_3Se_4 co-doped by Co and Fe.[39,40] This indicates that further exploration of the synergies between different 3d transition metals in these systems might enable the development of superior electrocatalysts. However, while moving toward the centers of multicomponent phase diagrams might bring certain benefits in terms of the catalytic activity, it also greatly enhances the number of possible material solutions, creating the necessity for utilizing effective, screening procedures, enabling the identification of the most promising directions of studies.

A particularly potent tool in this context are the so-called "electronic structure descriptors", which recently have been gaining a lot of interest with respect to a wide variety of reactions and technologies.[41–44] The main idea behind their application is that while most of the catalytic processes take place at the surface of the materials, their activity can be described by the bulk properties, originating from their electronic structure. Consequently, it is possible to assess the catalytic activity of the material, separately from the morphological features of the electrode. Such an approach not only provides means for effective evaluation of the catalytic activity, but also allows for effective screening of the materials with the use of *ab initio* calculations. By identifying the correlation between the redox potential of some of the most popular catalytic processes, such as OER and HER, the positions of TM d and the Ch p-orbital centers, together with the level of bonds covalency, have been identified as the most promising descriptors of catalytic activity.[41–43,45,46]

In the presented study, all the above-described subjects are brought together, leading to obtaining the highly active, multicomponent chalcogenides characterized by $(Co,Fe,Ni)_3Se_4$ stoichiometry. Based on the *ab initio* calculations and determined values of the most popular electronic structure descriptors, the potential benefits of utilizing near-equimolar mixtures of Co, Fe, and Ni 3d transitions metals are discussed, showing in the process the profound impact of multicomponent occupancy on the band structure of studied materials. Finally, based on this assessment, bulk $(Co,Fe,Ni)_3Se_4$ selenide characterized by metal-like properties is proposed and synthesized, followed by the characterization of its transport and electrochemical properties.

Experimental

The computational studies were performed using Vienna *ab initio* simulation package (VASP),[47] operating within the density functional theory (DFT) formalism. Structure relaxation was performed using 2 × 2 × 2 supercells (with as randomly as possible distributed Co, Fe, and Ni cations) in full optimization procedure (spin-polarization mode, unit cell parameters, atomic sites, and ionic relaxation), using the following criteria: generalized gradient approximation (GGA),[48] PBEsol[49] exchange-correlation potential, Monkhorst–Pack 2 × 5 × 3 *k*-point mesh, and 400 eV cut-off energy for plane wave basis sets. The Density of States (DOS) was generated on the basis of optimized model structures using a higher *k*-point mesh (4 × 10 × 6). Subsequently, the individual band centers were estimated as weighted average of the respective states.

For synthesis, high-purity elements in the form of powders (Co – 99.8% Alfa Aesar, Ni – 99.8% Alfa Aesar), granules (Fe – 99.98% Alfa Aesar), and pieces (Se – 99.999% Alfa Aesar) were weighted in the assumed ratios, initially homogenized, and sealed in double walled quartz ampoules under vacuum conditions (10^{-3} atm). The materials were synthesized from the as-prepared mixtures in a tube furnace by two-step heat treatment. Firstly, the ampules were heated up to 1273 K (1 K min^{-1}) and annealed for 24 h, with the reaction taking place in the liquid form (above the melting points of selenium). In the second step, the temperature was decreased to 773 K, where the ampule was annealed for another 72 h and quenched into the water (the conditions of the second step were determined experimentally through a series of syntheses). While even in the ingot form the materials were already suitable for the measurements, a considerable advantage by itself, the final materials were investigated in a form of sintered pellets. Here, the obtained ingots were subsequently milled into powder using a planetary mill (leading to the particle size at the level of 300–400 nm, as determined by dynamic light scattering measurements), and consolidated into disks (with a diameter of 10 mm and height of about 3 mm, for thermal and catalytic measurements) or cylinders (diameter of 10 mm and height of about 10 mm) by using inductive hot pressing (IHP) method.

The following procedure was applied during the IHP process: double rinsing with Ar (0.5 atm) at room temperature – heating up to 473 K (100 K min^{-1}) – annealing for 5 min – heating to 673 K (100 K min^{-1}) – annealing for 14 min under 50 MPa pressure, and for 1 min without pressure – cooling. The schematic representation of the synthesis procedure is provided in Fig. 1.

The density of the sintered pellets was examined with the use of Archimedes' principle and by volumetric measurements. The phase compositions of prepared samples (after synthesis and sintering process) were examined by means of X-ray diffraction (XRD) (apparatus: Empyrean PANanalytical apparatus (CuKα radiation)), and further analyzed with the use of X'Pert high score software. Microstructure observations and homogeneity of the samples were investigated by scanning electron microscopy combined with the energy-dispersive X-ray spectroscopy (SEM + EDS) (apparatus: Thermo Scientific Fisher Phenom XL scanning electron microscope equipped with EDS analyzer). The chemical composition of the obtained powder and sintered pellets were further studied by means of inductively coupled plasma optical emission spectroscopy (ICP-OES, apparatus Optima 7300DV ICP-OES spectrometer, PerkinElmer) and X-ray fluorescence spectroscopy (XRF, apparatus: Axios mAX spectrometer, PANalytical). For ICP-OES measurements, the samples were mineralized in concentrated HNO_3 at 523 K and 81 bar. For XRF measurements, the samples (2 g amounts) were mixed with micropowder c binder. The chemical state of elements was investigated by X-ray photoelectron spectroscopy (XPS). The measurements were conducted using the PHI VersaProbeII Scanning XPS system. The deconvolution of spectra was performed using PHI MultiPak software (v.9.9.2).

Samples for Mössbauer measurements were prepared in the form of a powder, embedded in epoxy resin, with the surface density of iron equal to 10 mg cm^{-2} ^{57}Fe Mössbauer spectra were recorded at 295 K in transmission mode using a standard spectrometer with a 57 Co/Rh source of 14.4 keV γ rays. Mössbauer spectra were analyzed assuming two independent quadrupole splitting (QS) distributions, with different QS ranges ad isomer shift (IS) values. It was assumed that the amounts of iron in individual crystallographic positions are proportional to the areas under the corresponding subspectra.

The electrical conductivity and Seebeck coefficient measurements were investigated by means of the DC 4-point van der Pauw method in the 293–723 K temperature range under He atmosphere.

Measurements of thermal properties, *i.e.*, thermal conductivity coefficient λ, determined on the basis of thermal diffusivity κ and specific heat C_p measurements – eqn (1).

$$\lambda = \kappa C_p \rho \quad (1)$$

where ρ – density of the samples, κ – thermal diffusivity, C_p – specific heat, were carried out with the use of the NETZSCH LFA 427 (laser flash analysis) and NETZSCH STA 449 F3 thermal analyzer, respectively, in the same temperature range of 293–723 K.

The electrochemical measurements were carried out with the use of M161 electrochemical analyzer (MTM-ANKO) at room temperature. A conventional three-electrode system was used, with $(Co,Fe,Ni)_3Se_4$ as the working electrode (custom-made holder), Pt + Pt black wire acting as an auxiliary one, and Ag/AgCl as the reference electrode. The electrochemical performance was assessed for polished (Al_2O_3-based polishing paste), sintered bulk material by connecting it directly to the Pt rod and placing it in a custom-made glass holder. The as-prepared electrode was sealed with silicone to ensure lack of contact between the electrolyte and Pt rod, and, at the same time, to ensure that surface of the pellet is in contact with the electrolyte without the involvement of lateral surfaces. Next, the $(Co,Fe,Ni)_3Se_4$ electrode was conditioned by several linear sweep voltammetric (LSV) cycles, with a scan rate of 200 mV s^{-1} in the range from −400 to 400 mV to achieve a steady state and

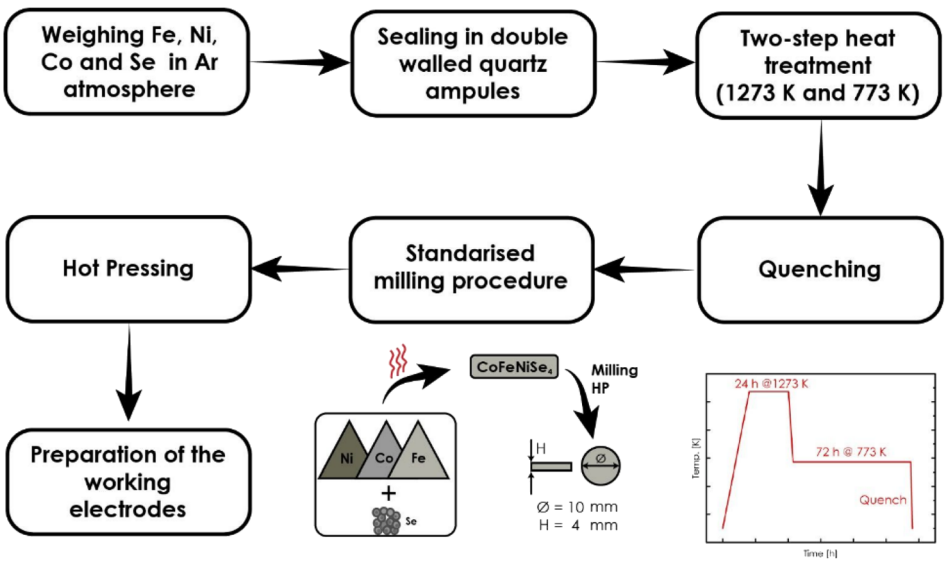

Fig. 1 Schematic representation of obtaining working electrode.

clear the surface from residual contaminations. In order to avoid overestimation of the obtained results, the electrochemical activity of the material was assessed on the basis of electrochemical active surface area (ECSA), instead of using geometric one (estimation of the available geometric surface area is limited by the accuracy of siliconization processes at the edge of the material-glassy holder connections). The ECSA was determined on the basis of electrochemical double-layer capacitance value (C_{dl}) from cyclic voltammetry measured in the 0–300 mV range and using 2.1–1000 mV s^{-1} scan rate.

Results and discussion

Electronic structure

Considering the relationship between electronic structure and electrochemical properties, the *ab initio* calculations were performed for a series of model structures, starting with the pseudo-spinels based exclusively on one of the following elements: Co, Fe, and Ni. Then, to provide a valid comparison, $(Co,Fe,Ni)_3Se_4$-based structures differing by Co, Fe, and Ni arrangement (Fig. 2), were evaluated. Due to the low symmetry of the system and only two available cationic sites, namely Wyckoff positions 2a/2d (multiplicity 1) and 4i (multiplicity 2), resulting in 2 non-equivalent cationic crystal sites per unit cell, it is impossible to create a 2 × 2 × 2 supercell (two 2a/2d sites with multiplicity 16 and four 4i sites with multiplicity 32) with three different cations occupying 2d positions. Thus, six model structures were designed with as random as possible arrangement of the cations in equimolar ratio, with the inevitable local ordering on 2d positions denoted as v1 (Fe in 2d sites, Fig. 2a), v2 (Co in 2d sites, Fig. 2b), v3 (Ni in 2d sites, Fig. 2c), v4 (Co and Ni in 2d sites, Fig. 2d), v5 (Co and Fe in 2d sites, Fig. 2e), and v6 (Fe and Ni in 2d sites, Fig. 2f). Worth noting, while the octahedron with TM in 2d sites is characterized by six equivalent TM–Se bonds (regular octahedron, slightly distorted depending on cations in 1st and 2nd coordination spheres, Fig. 2g), the octahedron with TM in 4i sites is characterized by six non-equivalent TM–Se bonds (non-regular octahedron with two types of bonds differing in average length, depending on the cations in 1st and 2nd coordination spheres, Fig. 2h).

The calculated structural parameters, together with the values of the electronic structure descriptors, are summarized in Table 1.

Computationally estimated unit cell parameters differ in all considered arrangements with the highest *a* parameter and unit cell volume corresponding to the v3 substructure, where only Ni occupies 2d sites. In general, the occupancy of 2d sites strongly influences the structural parameters, which is to be expected based on the trends observed for the unit cell parameters in monometallic systems.

The band structure and related density of states for all considered compositions and structures (Fig. 3 and 4), indicate a strongly metallic character with no band gap between the valence (VB) and conductance bands (CB) maxima, together with strong overlapping of the d states near the Fermi level. It seems clear that the semiconducting properties, including thermoelectric ones, can be expected to be poor. In terms of the catalytic properties, in order to assess the potential electrochemical activity the typical descriptors in the form of transition metal d-band center position d_b-c (as a weighted average of the respective states), and the gap between d_b-c and selenium center p_b-c, were calculated. It should be noted here, that the position of Se p_b-c band, similarly to oxides, can to some degree depend upon the presence of anion vacancies, shifting at the

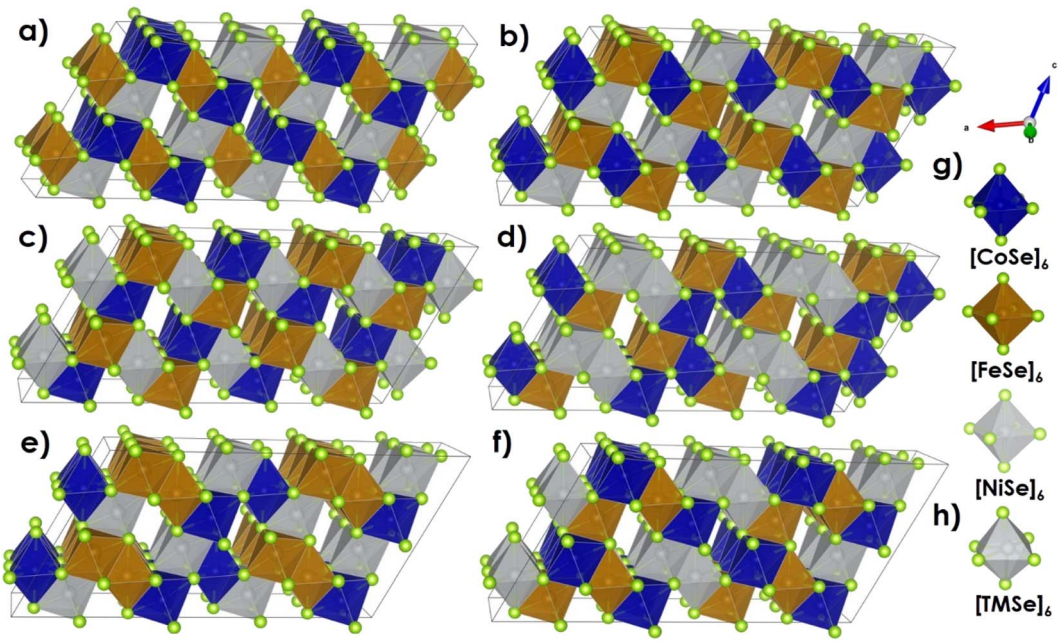

Fig. 2 Schematic representation of 2 × 2 × 2 $(Co,Fe,Ni)_3Se_4$ supercells denoted as v1 (a), v2 (b), v3 (c), v4 (d), v5 (e), and v6 (f); (g) $[TMSe]_6$ octahedron with TM in 2d site; (h) $[TMSe]_6$ octahedron with TM in 4i site.

Table 1 Estimated descriptors and structural parameters for $(Co,Fe,Ni)_3Se_4$ model structures differing by cation arrangements (where, d_b-c, p_b-c, and Δd-c–p_b-c denote to d-band center, p-band center, and the gap between d- and p-band centers respectively)

Structure	2d occ	4i occ	d_b-c [eV]	p_b-c [eV]	Δd_b-c–p_b-c [eV]	2d sites d_b-c [eV]	4i sites d_b-c [eV]	*a* param. [Å]	Cell vol. [Å^3]
Co_3Se_4	16Co	32Co	−1.19	−2.30	1.11	−1.20	−1.19	11.52	213.62
Fe_3Se_4	16Fe	32Fe	−0.84	−2.48	1.64	−0.83	−0.84	11.50	209.27
Ni_3Se_4	16Ni	32Ni	−1.83	−2.06	0.23	−1.76	−1.87	11.68	222.27
TM_3Se_4 v1	16Fe	16Co, 16Ni	−1.26	−2.15	0.89	−0.78	−0.84	11.55	216.03
TM_3Se_4 v2	16Co	16Fe, 16Ni	−1.20	−2.13	0.93	−1.16	−1.19	11.57	215.68
TM_3Se_4 v3	16Ni	16Co, 16Fe	−1.21	−2.12	0.92	−1.66	−0.98	11.76	218.46
TM_3Se_4 v4	8Co, 8Ni	8Co, 16Fe, 8Ni	−1.21	−2.12	0.92	−1.41	−1.09	11.65	217.23
TM_3Se_4 v5	8Co, 8Fe	8Co, 8Fe, 16Ni	−1.24	−2.17	0.93	−0.96	−1.37	11.51	215.17
TM_3Se_4 v6	8Fe, 8Ni	16Co, 8Fe, 8Ni	−1.21	−2.11	0.90	−1.20	−1.22	11.66	217.51

same time TM d-band centers.[43] However, the effects associated with their presence are usually outside of the experimental measuring range. Thus, computational studies focused only on stoichiometric $(Co,Fe,Ni)_3Se_4$ will be taken into account.

The density of states (DOS) plots for monometallic selenides (Fig. 3), indicate that among the Co_3Se_4, Fe_3Se_4, and Ni_3Se_4 compounds, if only the d-band is considered, the iron-rich composition should be the most catalytically active, as evidenced by the position of iron d_b-c being the closest to the Fermi level (−0.84 eV), while the Ni_3Se_4 can be expected to be the least active one (−1.83 eV). Notably, for monometallic compounds, the position of d band centers is nearly identical for states associated with 2d or 4i sites, respectively (Table 1). On the other hand, Ni_3Se_4 is characterized by the closest to Fermi level p_b-c, as well as the lowest distance between the centers of the TM d-band and the Se p-band centers (Δd_b-c–p_b-c) equal to 0.23 eV, while Fe_3Se_4 has the largest, which points to an exactly opposite relation between their activities. It is hard to confirm which descriptor is more effective here, due to the insufficient amount of available data, combined with the lack of consistency between different studies. It seems, however, that among those three monometallic selenides with monoclinic stoichiometry, the cobalt-rich samples with intermediate values of both d_b-c and Δd_b-c–p_b-c, should be the most exciting for electrochemical water splitting processes.[38,50] Further modification of the properties of these monometallic compounds can be performed by doping/mixing of different cations, which has been widely reported as beneficial for their catalytic performance.[39,40]

The presented herewith case takes the most radical approach to this subject, with an equimolar, ternary mixture of Co, Fe, and Ni being considered, with results strongly supporting the notion of the prominent impact of multicomponent occupancy. Firstly, the coexistence of two or more cations strongly influences the overlapping of the d-states near the Fermi level (Fig. 4), providing a high charge carrier concentration and thus high electrical conductivity and fast charge transfer. Synergistic effects between cations also affect the relatively high occupation of antibonding d-orbitals near the Fermi level, further contributing to fast charge transfer and prominent catalytic activity.

In terms of the descriptors, surprisingly, the high occupation of anti-bonding d orbitals near d_b-c and p_b-c centers does not clearly shift respective d_b-c toward the Fermi level as might be expected. The respective positions of d-states, as well as d-band centers related to individual TM, do not overlap, but retain their position leading to the following sequence: Ni states – Co states – Fe states – Fermi level. Thus, the center of the d-band related to all TM is an average value of the 3 individual band centers, with the effective value being similar to the one of monometallic Co_3Se_4. However, in contrary to monometallic compounds, the positions of band centers associated with 2d and 4i sites, might differ considerably within a given structure, depending on the relative distribution of the cations. Thus, for certain types of distributions, one might be able to exploit the benefits of

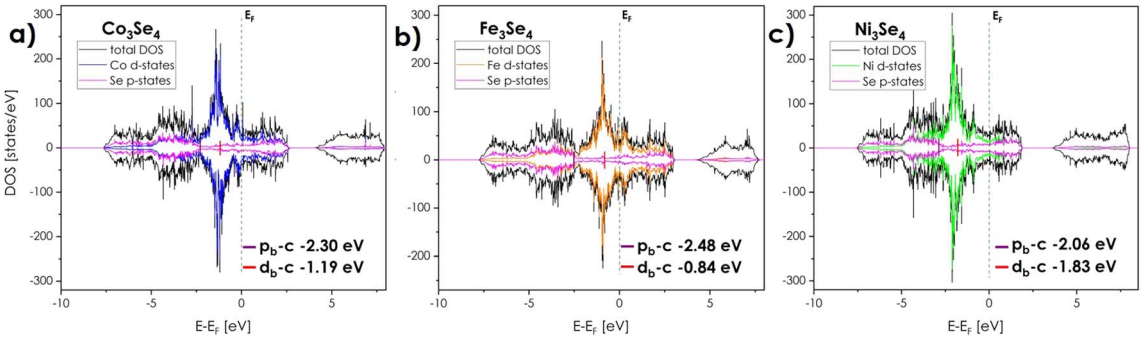

Fig. 3 Total and partial density of states: (a) Co_3Se_4; (b) Fe_3Se_4; (c) Ni_3Se_4.

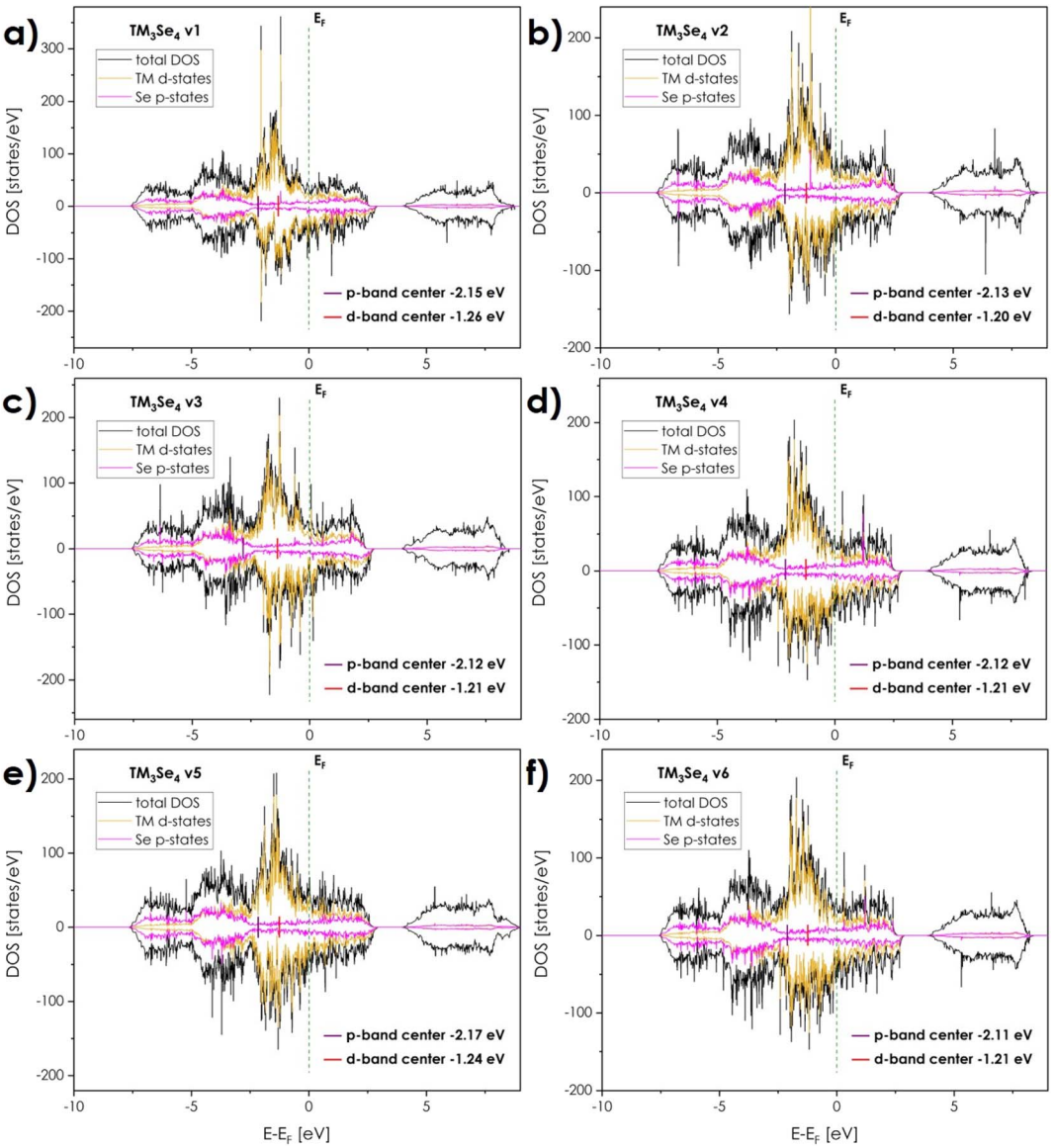

Fig. 4 Total and partial density of states for $(Co,Fe,Ni)_3Se_4$ structures: (a) v1 with only Fe cations in 2d sites, (b) v2 with only Co cations in 2d sites, (c) v3 with only Ni cations in 2d sites, (d) v4 with a combination of Co and Ni cations in 2d sites, (e) v5 with a combination of Co and Fe cations in 2d sites, (f) v6 with a combination of Fe and Ni cations in 2d sites.

different monometallic compounds within a single composition. Based on such presumption, it can be postulated that indeed iron in the 4i position and nickel in the 2d position are the most favorable arrangement strongly influencing the positions of the d-band (Fe in 4i sites) and p-band centers (Ni in 2d sites), respectively. Simultaneously, the selenium p-band center is moving toward the Fermi level for all multicationic systems, decreasing the Δd_b-c–p_b-c gap to the level suggesting that independent from the specific cationic arrangement, the overall catalytic activity of $(Co,Fe,Ni)_3Se_4$ should be better in relation to monometallic systems apart from Ni_3Se_4 one. Again, the presence of Ni cations in 2d sites shifts p-band center towards Fermi level, which translates into a further narrowing of Δd_b-c–p_b-c gap and thus it seems justified to conclude that Ni located mostly in 2d sites should be the most beneficial. It remains to be seen, whether the considered, equimolar composition corresponds to the optimum of catalytic activity, with the non-equimolar or binary combinations of 3d TM being potentially equally effective. Still, the potential benefits of the multicomponent approach are evident. A detailed investigation aimed at the identification of the most effective descriptors combined with experimental verification for mono- and bimetallic systems will be a direct continuation of the presented study.

Structural studies

To exploit the features of the multicomponent occupancy, the $(Co,Fe,Ni)_3Se_4$ compound based on all three (Co, Fe, and Ni) cations in the equimolar ratio was successfully obtained for the first time (Fig. 5a). Worth noting, all attempts of obtaining the selected compositions on the basis of wet chemistry methods

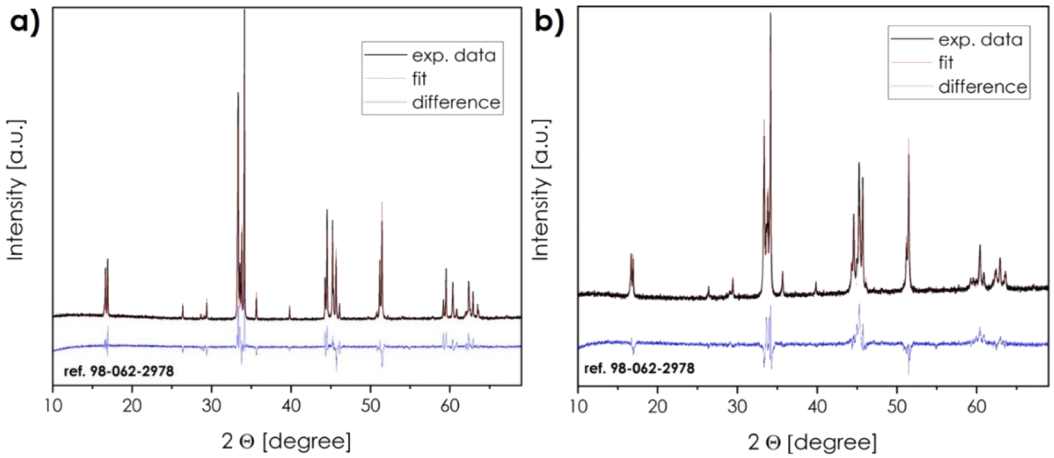

Fig. 5 XRD patterns for (a) $(Co,Fe,Ni)_3Se_4$ powder (GoF 8.56, wRp 7.81) and (b) $(Co,Fe,Ni)_3Se_4$ sintered pellet (GoF 5.75, wRp 5.51) samples respectively.

failed (similarly as for high-entropy pentlandites[29]), indirectly confirming the notion of strongly metallic properties of the material, see previous section.

The proposed sintering process with empirically determined conditions allows obtaining bulk material with a density at the level of 6.45 g cm^{-3} (which is about 93% of relative density, considering a theoretical density of about 6.95 g cm^{-3}) and does not impact negatively the crystal structure of the material (Fig. 5b). SEM micrographs of the sintered materials together with EDS results prove high homogeneity and equimolar distribution of cations in the material, indicating high stability under temperature and mechanical stress (Fig. 6). The more detailed chemical composition studies performed using ICP-OES and XRF methods, further confirmed the close-to-nominal ratios of the elements, with the established general formulae for respective samples and methods being: $Co_{0.96}FeNi_{0.94}Se_{3.96}$ (ICP-OES powder), $CoFeNi_{1.04}Se_{4.16}$ (ICP-OES pellet), $Co_{0.96}FeNi_{1.02}Se_{3.82}$ (XRF powder), and $Co_{0.96}FeNi_{1.06}Se_{4.04}$ (XRF pellet) (see also ESI Table 1†).

Based on the theoretical results, the occupancy of iron and nickel is of primary importance to the material's potential with regard to catalysis. In order to study the structural trends within the proposed Co–Fe–Ni–Se system, all 6 binary combinations of the selected cations were also synthesized (ESI Fig. 1†). Based on the values of lattice parameters (Table 2), it can be stated that only iron ions tend to occupy locally ordered crystal sites, as evidenced by a clear expansion of the unit cell along the [100], Table 2. Combining these observations with computational studies, it should be expected that the relatively big iron cations may indeed occupy the desired 4i sites, increasing cell parameters and simultaneously forcing Ni or Co to occupy the preferred 2d sites.

Table 2 Basic structural data together with fitting indices obtained from XRD measurements for bi- and trimetallic selenides

Chem. composition	a [Å]	b [Å]	c [Å]	β [°]	GoF	wRp
$FeNi_2Se_4$	12.19	3.58	6.16	118.94	11.81	10.24
$Fe_{1.5}Ni_{1.5}Se_4$	12.29	3.59	6.16	118.41	10.43	9.07
Fe_2NiSe_4	12.40	3.56	6.17	117.99	8.97	8.36
$CoNi_2Se_4$	12.02	3.61	6.16	119.51	5.68	6.47
$Co_{1.5}Ni_{1.5}Se_4$	12.03	3.60	6.16	119.42	5.24	5.45
Co_2NiSe_4	12.00	3.59	6.15	119.26	4.39	4.56
$CoFe_2Se_4$	12.38	3.54	6.15	117.90	2.40	3.56
$Co_{1.5}Fe_{1.5}Se_4$	12.28	3.55	6.16	118.01	7.95	6.33
Co_2FeSe_4	12.15	3.56	6.14	118.54	4.56	4.86
$CoFeNiSe_4$ powder	12.18	3.57	6.15	118.67	8.56	7.81
$CoFeNiSe_4$ pellet	12.18	3.57	6.15	118.66	5.75	5.51

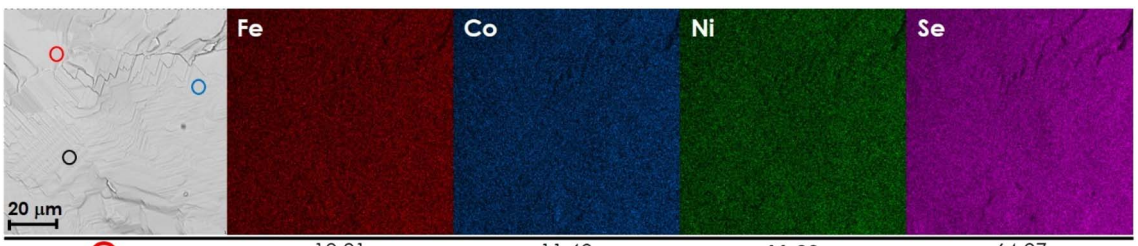

○	12.21	11.69	11.83	64.27
○	12.39	12.11	12.38	63.12
○	12.57	11.86	12.54	63.03
average	12.49	11.90	12.22	63.39

Fig. 6 SEM micrograph together with EDS point and map analysis of the cross-section $(Co,Fe,Ni)_3Se_4$ sintered sample.

The positions and valence states of the cations were also investigated using spectroscopic methods. As visible from the XPS spectra (see ESI Fig. 2 and 3†), all cations appear to exhibit a certain level of TM^{2+}/TM^{3+} multivalency, although it should be noted that due to the similarities between the positions of peaks for different transition metals, it is hard to draw unambiguous conclusions regarding the valence state of each of them.[28,40,51,52] Furthermore, due to the surface-sensitive nature of the measurement, the obtained data might not correspond to the bulk properties of the material. Therefore, to address the essential question of Fe ions position, the Mössbauer spectroscopy measurements were also performed. Fig. 7a shows the Mössbauer spectrum of the $(Co,Fe,Ni)_3Se_4$ sample recorded at room temperature. Estimated isomer shift values equal to 0.48 (±0.02) and 0.42 (±0.02) correspond to Fe^{3+} coexisting in octahedral sites at the Wyckoff positions 2d and 4i, respectively.[53,54] Due to the lack of magnetism at this temperature, as well as the occurrence of Ni and Co in different neighborhood configurations in relation to Fe, the structure of the spectrum is blurred and allows only two Gaussian distributions. However, the quadrupole splitting distribution (Fig. 7b) indicates that only 25% of iron occupies 2d sites, while 75% Fe cations occupy 4i sites (in the ideal $(Co,Fe,Ni)_3Se_4$ structure this ratio should be 1 : 2). This 1 : 4 ratio, instead of 1 : 2, confirms certain preference of iron cations to occupy 4i, and agrees well with the structural data. In such an arrangement, the excess of Co and Ni ions would be expected at the 2d sites, corresponding well to the potentially beneficial features identified during theoretical calculations.

Transport properties

The total electrical conductivity together with the values of the Seebeck coefficient are presented as a function of temperature in Fig. 8. Based on the obtained results, the initial assumptions concerning the highly metallic character of $(Co,Fe,Ni)_3Se_4$ selenide seem to be justified, as evidenced by high values of electrical conductivity at the level of 8.5–9 10^4 Sm^{-1}, which is higher than in the most of TMCh, including copper-based chalcogenides[1] or chalcogenides characterized by spinel structure,[55] and at a comparable level to multicomponent pentlandites.[29] The observed values of electrical conductivity can be related to high charge carrier concentration, providing more than enough charge transfer capabilities for successful electrode operation. Assuming the metallic character (or, alternatively, strongly degenerated semiconductor behavior) of the sample, the electrical conductivity should decrease with temperature. However, the electrical conductivity does not indicate any clear monotonicity, taking almost constant values across the considered temperature range, which is probably related to the high concentration of minority charge carriers. Considering only the 2nd cycle, the decrease of the electrical conductivity with temperature can be noticed up to 400–450 K, similarly as for high-entropy pentlandites.[29]

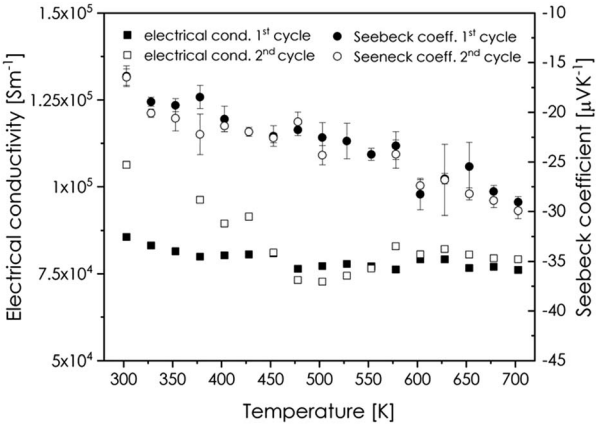

Fig. 8 Electrical conductivity and Seebeck coefficient as a function of temperature of the $(Co,Fe,Ni)_3Se_4$ sample.

The presumption of the metallic character of the material is also consistent with the relatively small values of the Seebeck coefficient at the level of −20 μV K^{-1} at RT, only slightly increased at higher temperatures. Here, the increase of the Seebeck coefficient with temperature is clearly related to the decreasing mobility of the cations with temperature. In contrary to pentlandites that tend to be p-type conductors, $(Co,Fe,Ni)_3Se_4$ selenides exhibit negative values of the Seebeck coefficient, which is to be expected considering the formal and averaged charge of the TM equal to +2.67 (for stoichiometric composition).

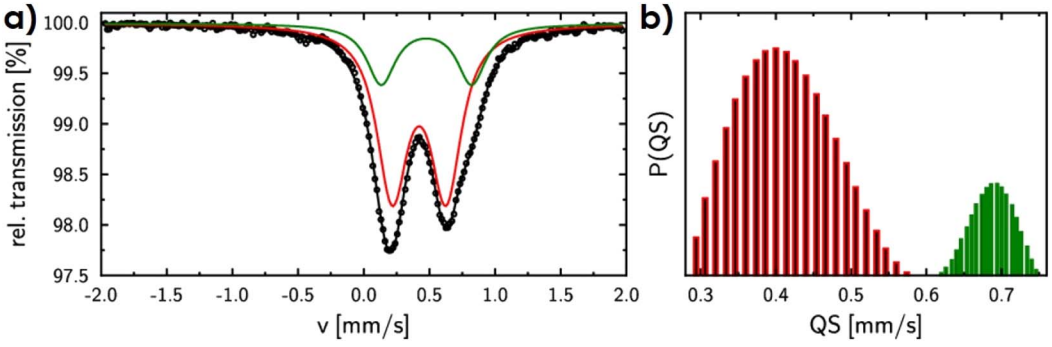

Fig. 7 (a) Mössbauer spectrum of $(Co,Fe,Ni)_3Se_4$. Black points and lines correspond to the experimental data. Red and green lines denote individual Fe subspectra; (b) quadrupole splitting distribution of the respective Fe subspectra.

Further evaluation of the material included thermal and thermoelectric properties, with the results being available in ESI, see ESI Fig. 4.† In general, while the material exhibits surprisingly low values of thermal conductivity of 2.6 W m^{-1} K^{-1} at RT, its thermoelectric performance is still largely compromised by low values of the Seebeck coefficient, resulting in the thermoelectric figure-of-merit value of *ca.* 0.01 at 675 K, practically excluding $(Co,Fe,Ni)_3Se_4$ selenides and related materials from thermoelectric applications, at least in the current, undoped state.

Electrocatalytic properties

The results of the electrocatalytic performance assessment of the $(Co,Fe,Ni)_3Se_4$ electrode are summarized in Fig. 9, Tables 3 and 4. Fig. 9a shows the LSV curves of the $(Co,Fe,Ni)_3Se_4$ electrode towards HER, recorded at 6.25 mV s^{-1} and normalized with respect to ECSA, *versus* the reversible hydrogen electrode (RHE) (for the LSV curve presented as a function of geometrical surface area, see ESI Fig. 5†). The results for Pt and $Fe_{4.5}Ni_{4.5}S_8$ electrodes are also provided for reference. It should be noted that similar as in the case of Konkena *et al.*,[28] bulk-type electrodes were considered, in order to prove the potential of the studied material to operate without needing expensive and time-consuming electrode layer preparation. Due to this, the recorded current densities values are relatively high, making it difficult to directly compare with the literature data. Also, the residual cathodic current is present (related probably with residual reactions involving Se anions on the materials surface, charge compensating from Se vacancies, or may be somehow connected to the not ideal surface roughness and naturally (randomly) crystallized crystallographic planes), therefore overpotential values at 120, 500, and 1000 mA cm^{-2} are presented in Table 3, rather than at the more common value of

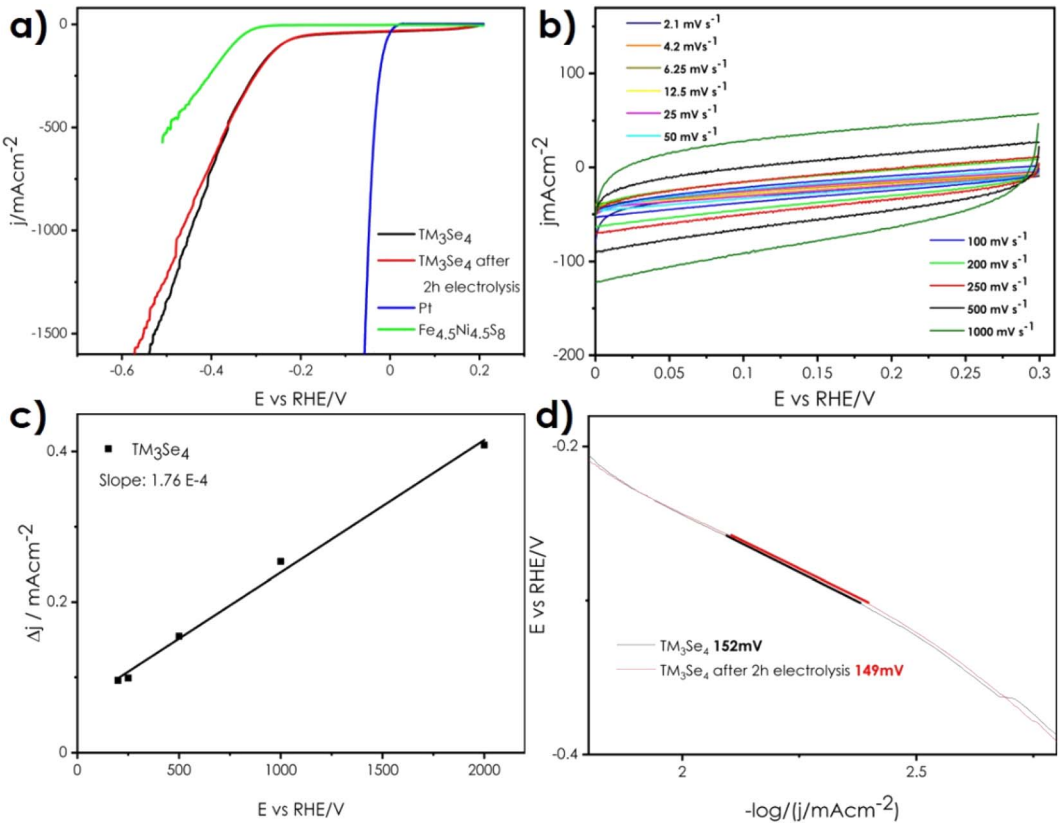

Fig. 9 (a) Linear sweep voltammograms of the $(Co,Fe,Ni)_3Se_4$ catalyst recorded at sweep rate 6.25 mV s^{-1} in 0.5 M H_2SO_4. The diffusion limited current densities was normalized to the ECSA. Bulk pentlandite result added as a comparison; (b) cyclic voltammograms of $(Co,Fe,Ni)_3Se_4$ electrode; (c) charging current densities as a function of scan rate; (d) Tafel plots derived from voltammograms at sweep rate 6.25 mV s^{-1}.

Table 3 Basic electrocatalytical performance presented as overpotential *vs.* RHE as a function of current density

Chemical composition (initial particle size 300–400 nm)	Overpotential at 120 mA cm^{-2} [mV] *vs.* RHE		Overpotential at 500 mA cm^{-2} [mV] *vs.* RHE		Overpotential at 1000 mA cm^{-2} [mV] *vs.* RHE	
	1st cycle	After 2h	1st cycle	After 2h	1st cycle	After 2h
$CoFeNiSe_4$	255	255	361	364	448	467

Table 4 Overpotentials at certain current densities for $CoFeNiSe_4$ solid electrodes *versus* chosen literature data

Sample	Overpotential [mV]				Reference
	At 10 mA cm^{-2}	At 50 mA cm^{-2}	At 100 mA cm^{-2}	At 400 mA cm^{-2}	
$CoFeNiSe_4$ (normalized to ECSA)	—	180	244	342	This work
$CoFeNiSe_4$ (normalized to geom. area)	245	365	447	—	This work
Pt (normalized to ECSA)	0	2	12	30	This work
Pt (normalized to geom. area)	86	208	—	—	This work
$Fe_{4.5}Ni_{4.5}S_8$ (normalized to ECSA)	292	332	355	—	This work
$Fe_{4.5}Ni_{4.5}S_8$	319	385	—	—	28 and 58
$Co_3Fe_3Ni_3S_8$	285	376	—	—	58
$Fe_{4.5}Ni_{4.5}S_4Se_4$	~320	~395	—	—	30
Ni_3Se_4/CC	~100	~240	~350	—	40
$Ni_{1.86}Co_{1.05}Fe_{0.09}Se_4$/CC	~87	~200	~300	—	40
Ni_3Se_4@$MoSe_2$	242	~300	—	—	59

10 mA cm^{-2}.[56] As can be seen, the reaction starts in the overpotential range of 215–240 mV, reaching a current density equal to −120 μA cm^{-2} at 255 mV, and −500 mA cm^{-2} at 361 mV, indicating excellent HER activity. The obtained material also compares well to other monometallic selenides, *e.g.*, Ni_3Se_4 or Ni_3Se_4 co-doped by Co and Fe (as nanomaterials on carbon cloth), where a typical current density value of −10 mA cm^{-2} is reached at an overpotential of about 100 mV, while −120 μA cm^{-2} is reached at 380 and 300 mV respectively[40] (Table 4). What is even more interesting, is the comparison with the bulk $Fe_{4.5}Ni_{4.5}S_8$ pentlandite electrode, which by itself can be considered a major breakthrough.[28] As presented in Fig. 9a, the performance of $(Co,Fe,Ni)_3Se_4$ is superior by a considerable margin, making it likely the best-performing bulk electrode up to date. This spectacular performance is a direct result of both the intrinsic properties of the material and sample processing. The intrinsic properties of $(Co,Fe,Ni)_3Se_4$ stem from at least three phenomena: electronic structure and related synergistic effects provided by multi occupied cationic sublattice, high concentration of active sites corresponding to intermetallic interactions, and electrical high conductivity of the material. Sample processing, in turn, provides high density, improving charge transfer capabilities, and ensuring a high level of Se vacancies at the surface (as a result of Se evaporating during sintering[1,57]).

Based on the CV results (Fig. 9b), the linear regression of charging current densities representing double layer capacitance (C_{dl}) (that is proportional to ECSA, Fig. 9c) was estimated. Usually, the larger ECSA, the more available active sites and increased HER activity is expected. For transition metal chalcogenides in which TM-Ch bridges occur, the ECSA is larger in comparison to $TMCh_2$ structures, which is related to efficient H adsorption mechanism at the intermetallic Ch vacancies sites.[28,31] Here, values similar or slightly lower than those presented for various chalcogenide catalysts can be identified,[22,51] which is probably related to both high Se content (similarly as for other TM_3Se_4 composition[51]) and specific sample form.

Presented in Fig. 9d Tafel plot of $(Co,Fe,Ni)_3Se_4$ electrode, indicates relatively high values of Tafel slope at the level of 150 mV dec^{-1}, suggesting the presence of Volmer–Heyrovski kinetic mechanism of H_2 evolution instead of the preferred Volmer–Tafel one, typical for Pt and other noble-based catalysts.

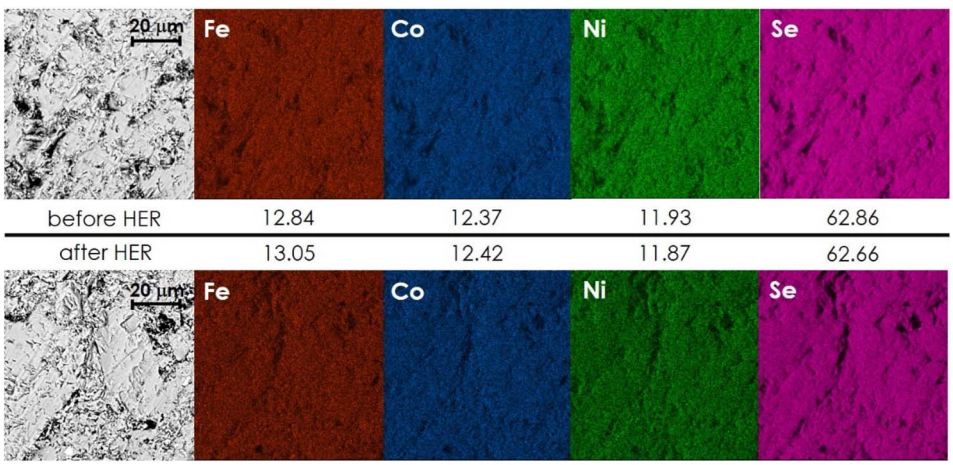

Fig. 10 SEM micrograph together with EDS map analysis of the $(Co,Fe,Ni)_3Se_4$ sintered sample surfaces before (top) and after (bottom) electrochemical testing.

It is likely that for the studied $(Co,Fe,Ni)_3Se_4$ electrode, the proton adsorption step (Volmer) is the limiting one, due to both the high concentration of selenium,[30] and the form of the sample. It is also in line with a relatively high overpotential, where the chemisorption of hydrogen by the metal is favored. Worth noting, the literature data for monometallic TM_3Se_4 nanomaterials suggest significantly lower values of the Tafel slope, at the level of 40–50 mV dec^{-1},[38] indicating the dominant influence of sample morphology on the H_2 evolution mechanism. It is also possible that the working surface of the sample is somewhat contaminated by residual oxygen connected to the cations with uncompensated charge (high concentration of Se vacancies). In such a case it is reasonable to suspect the presence of certain TM–O– intermediates or the electrolyte penetration through the working electrode that may affect the kinetics of HER, which is consistent with nonzero cathodic currents. Nevertheless, taking into account the observed, very high level of HER catalytic activity, it can be said that the presented approach, aimed at maximizing the simplicity of the manufacturing process (without any artificial nanostructuring), as well as increased mechanical and catalytical durability (see HER performance after 2 h of electrolysis, Fig. 9d, and XRD/SEM results before/after electrochemical characterization, Fig. 5b, 6, and 10, ESI Fig. 6†), can be considered highly successful in the case of the studied $(Co,Fe,Ni)_3Se_4$ material. Moreover, the design of the material itself, concentrated on exploiting synergies between different transition metal elements deserves special attention, as not only it is already characterized by excellent catalytic performance, but can also serve as a starting point for further improvements, by tailoring the ratios of the composing cations, a process which can be further supported by the use of theoretical calculations utilizing electronic structure descriptors.

Conclusions

In this work, trimetallic $(Co,Fe,Ni)_3Se_4$ pseudospinel selenide characterized by equimolar Co : Fe : Ni ratio and monoclinic *C*2/*m* structure is presented for the first time. Based on the performed theoretical DFT calculations, the band structure of the material is investigated for different, possible atomic arrangements, together with the preliminary assessment of the catalytic activity for each of them, based on the electronic structure descriptors. The results indicate that the application of the multicomponent approach might contribute to enhanced catalytic activity of such compound compared to its monometallic counterparts, by combining their strongest positive traits, while minimizing the impact of negative ones. The arrangement combining the excessive number of Ni cations at the 2d sites, and Fe at the 4i sites, is identified as the most favorable.

The experimental, structural data, together with the XPS and Mössbauer spectroscopy results, strongly suggest that such an arrangement may indeed take place in the $(Co,Fe,Ni)_3Se_4$ material, with a notable preference of Fe cations towards occupying the 4i sites forcing other two cations into the 2d ones. The transport properties indicate excellent charge-transfer capabilities and the metallic character of the studied compound. Interestingly, the thermal conductivity of this material is very low, which is probably related to a multivalley electronic structure and an additional phonon scattering mechanism related to multi-occupied sublattices and local structural distortions of the structure.

The catalytic activity with regard to HER is also assessed, with the application of bulk-type electrode, a feature of considerable, economic implications. Despite the relatively low electrochemical active surface area and rather unfavorable kinetics of the H_2 evolution, inherently correlated with such geometry of the electrode, the material offers excellent HER performance, evidenced by reaching very high current densities at low overpotentials (250 mV at 120 mA cm^{-2}, 360 mV at 500 mA cm^{-2}, and 450 mV at 1000 mA cm^{-2}, respectively). What is more, the material is characterized by good stability under operating conditions, stemming from both intrinsic material properties and the electrode's processing.

The proposed approach, combing the multicomponent approach to materials design, application of the theoretical descriptors of catalytic activity, and usage of cheap and scalable methods of electrode production, allowed obtaining a highly active, stable, and affordable $(Co,Fe,Ni)_3Se_4$ electrocatalyst. Based on the intrinsic properties of this material, it can be expected that its reported, already excellent performance can be further improved either by tailoring the ratios of the composing cations or by application of more refined methods of electrode preparation, whenever justified by economic factors.

Author contributions

Andrzej Mikuła: conceptualization, data curation, formal analysis, funding acquisition, investigation, methodology, project administration, resources, supervision, validation, visualisation, writing – original draft, writing – review & editing. Juliusz Dąbrowa: supervision, formal analysis, validation, writing – review & editing, writing – review & editing. Jakub Cieślak: investigation, formal analysis, visualization. Maciej Kubowicz: data curation, formal analysis, investigation, methodology, visualization. Wiktor Lach: investigation. Miłosz Kożusznik: investigation, visualisation. Mathias Smialkowski: methodology, formal analysis, validation. Ulf-peter Apfel: supervision, formal analysis, validation, writing – review & editing.

Conflicts of interest

There are no conflicts to declare.

Acknowledgements

Ulf-Peter Apfel was funded by the Deutsche Forschungsgemeinschaft (DFG, German Research Foundation) under Germany's Excellence Strategy – EXC 2033 – 390677874 – RESOLV as well as APAP242/9-1, the Fraunhofer Internal Programs under Grant no. Attract 097-602175. The authors are also thankful for support by the Mercator Research Center Ruhr

(MERCUR.Exzellenz, 'DIMENSION' Ex-2021-0034 and 'Kata-Sign' Ko-2021-0016). This work was financially supported by the National Science Centre, Poland, under grant no. 2022/45/B/ST8/03336. We gratefully acknowledge Poland's high-performance computing infrastructure PLGrid (HPC Centers: ACK Cyfronet AGH) for providing computer facilities and support within computational grant no. PLG/2021/015239.

Notes and references

1 P. Qiu, X. Shi and L. Chen, *Energy Storage Mater.*, 2016, **3**, 85–97.
2 I. Pallecchi, N. Manca, B. Patil, L. Pellegrino and D. Marré, *Nano Futures*, 2020, **4**, 032008.
3 D. Yang, X. Su, J. Li, H. Bai, S. Wang, Z. Li, H. Tang, K. Tang, T. Luo, Y. Yan, J. Wu, J. Yang, Q. Zhang, C. Uher, M. G. Kanatzidis and X. Tang, *Adv. Mater.*, 2020, **32**, 2003730.
4 A. Mikuła, P. Nieroda, K. Mars, J. Dąbrowa and A. Koleżyński, *Solid State Ionics*, 2020, **350**, 115322.
5 P. Nieroda, J. Leszczyński, A. Mikuła, K. Mars, M. J. Kruszewski and A. Koleżyński, *Ceram. Int.*, 2020, **46**, 25460–25466.
6 D. L. Shi, Z. M. Geng, L. Shi, Y. Li and K. H. Lam, *J. Mater. Chem. C*, 2020, **8**, 10221–10228.
7 S. O. J. Long, A. V. Powell, P. Vaqueiro and S. Hull, *Chem. Mater.*, 2018, **30**, 456–464.
8 K. Suekuni, K. Tsuruta, M. Kunii, H. Nishiate, E. Nishibori, S. Maki, M. Ohta, A. Yamamoto and M. Koyano, *J. Appl. Phys.*, 2013, **113**, 043712.
9 J. H. Pi, S. G. Kwak, S. Y. Kim, G. E. Lee and I. H. Kim, *J. Electron. Mater.*, 2019, **48**, 1991–1997.
10 K. Zhao, P. Qiu, X. Shi and L. Chen, *Adv. Funct. Mater.*, 2020, **30**, 1903867.
11 R. Woods-Robinson, Y. Han, H. Zhang, T. Ablekim, I. Khan, K. A. Persson and A. Zakutayev, *Chem. Rev.*, 2020, **120**, 4007–4055.
12 M. R. Gao, Y. F. Xu, J. Jiang and S. H. Yu, *Chem. Soc. Rev.*, 2013, **42**, 2986–3017.
13 K. Michalec and A. Kusior, *Molecules*, 2021, **26**, 7123.
14 B. Yun, H. Zhu, J. Yuan, Q. Sun and Z. Li, *J. Mater. Chem. B*, 2020, **8**, 4778–4812.
15 X. Chen, J. Yang, T. Wu, L. Li, W. Luo, W. Jiang and L. Wang, *Nanoscale*, 2018, **10**, 15130–15163.
16 J. Yin, J. Jin, H. Lin, Z. Yin, J. Li, M. Lu, L. Guo, P. Xi, Y. Tang and C. Yan, *Adv. Sci.*, 2020, **7**, 1903070.
17 X. Chen, J. Yang, T. Wu, L. Li, W. Luo, W. Jiang and L. Wang, *Nanoscale*, 2018, **10**, 15130–15163.
18 M. Ďurovič, J. Hnát and K. Bouzek, *J. Power Sources*, 2021, **493**, 229708.
19 F. Te Tsai, Y. T. Deng, C. W. Pao, J. L. Chen, J. F. Lee, K. T. Lai and W. F. Liaw, *J. Mater. Chem. A*, 2020, **8**, 9939–9950.
20 N. T. Suen, S. F. Hung, Q. Quan, N. Zhang, Y. J. Xu and H. M. Chen, *Chem. Soc. Rev.*, 2017, **46**, 337–365.
21 J. Song, C. Wei, Z. F. Huang, C. Liu, L. Zeng, X. Wang and Z. J. Xu, *Chem. Soc. Rev.*, 2020, **49**, 2196–2214.
22 N. Dubouis and A. Grimaud, *Chem. Sci.*, 2019, **10**, 9165–9181.
23 X. Geng, W. Sun, W. Wu, B. Chen, A. Al-Hilo, M. Benamara, H. Zhu, F. Watanabe, J. Cui and T. Chen, *Nat. Commun.*, 2016, **7**, 10672.
24 R. Miao, B. Dutta, S. Sahoo, J. He, W. Zhong, S. A. Cetegen, T. Jiang, S. P. Alpay and S. L. Suib, *J. Am. Chem. Soc.*, 2017, **139**, 13604–13607.
25 F. Ma, Y. Liang, P. Zhou, F. Tong, Z. Wang, P. Wang, Y. Liu, Y. Dai, Z. Zheng and B. Huang, *Mater. Chem. Phys.*, 2020, **244**, 122642.
26 X. Chia, A. Ambrosi, Z. Sofer, J. Luxa and M. Pumera, *ACS Nano*, 2015, **9**, 5164–5179.
27 Y.-R. Zheng, M.-R. Gao, Q. Gao, H.-H. Li, J. Xu, Z.-Y. Wu and S.-H. Yu, *Small*, 2015, **11**, 182–188.
28 B. Konkena, K. J. Puring, I. Sinev, S. Piontek, O. Khavryuchenko, J. P. Dürholt, R. Schmid, H. Tüysüz, M. Muhler, W. Schuhmann and U. P. Apfel, *Nat. Commun.*, 2016, **7**, 1–8.
29 A. Mikuła, J. Dąbrowa, A. Kusior, K. Mars, R. Lach and M. Kubowicz, *Dalton Trans.*, 2021, **50**, 9560–9573.
30 M. Smialkowski, D. Siegmund, K. Pellumbi, L. Hensgen, H. Antoni, M. Muhler and U. P. Apfel, *Chem. Commun.*, 2019, **55**, 8792–8795.
31 I. Zegkinoglou, A. Zendegani, I. Sinev, S. Kunze, H. Mistry, H. S. Jeon, J. Zhao, M. Y. Hu, E. E. Alp, S. Piontek, M. Smialkowski, U.-P. Apfel, F. Körmann, J. Neugebauer, T. Hickel and B. Roldan Cuenya, *J. Am. Chem. Soc.*, 2017, **139**, 14360–14363.
32 M. Smialkowski, D. Tetzlaff, L. Hensgen, D. Siegmund and U.-P. Apfel, *Chin. J. Catal.*, 2021, **42**, 1360–1369.
33 S. Hébert, T. Barbier, D. Berthebaud, O. I. Lebedev, V. Pralong and A. Maignan, *J. Phys. Chem. C*, 2021, **125**, 5386–5391.
34 H. M. A. Amin, M. Attia, D. Tetzlaff and U. Apfel, *ChemElectroChem*, 2021, **8**, 3863–3874.
35 L. Lu, S. Yu and H. Tian, *J. Colloid Interface Sci.*, 2022, **607**, 645–654.
36 X. Li, K. Zheng, J. Zhang, G. Li and C. Xu, *ACS Omega*, 2022, **7**, 12430–12441.
37 T. Wu, Y. Sun, X. Ren, J. Wang, J. Song, Y. Pan, Y. Mu, J. Zhang, Q. Cheng, G. Xian, S. Xi, C. Shen, H. Gao, A. C. Fisher, M. P. Sherburne, Y. Du, J. W. Ager, J. Gracia, H. Yang, L. Zeng and Z. J. Xu, *Adv. Mater.*, 2023, **35**, 2207041.
38 W. Li, X. Gao, D. Xiong, F. Wei, W.-G. Song, J. Xu and L. Liu, *Adv. Energy Mater.*, 2017, **7**, 1602579.
39 R. Balaji, J. Balamurugan, T. T. Nguyen, N. H. Kim and J. H. Lee, *Chem. Eng. J.*, 2020, **390**, 124557.
40 C. Zhou, H. Wu, F. Zhang and Y. Miao, *Crystals*, 2022, **12**, 666.
41 Y.-L. Lee, J. Kleis, J. Rossmeisl, Y. Shao-Horn and D. Morgan, *Energy Environ. Sci.*, 2011, **4**, 3966.
42 H. Lee, O. Gwon, K. Choi, L. Zhang, J. Zhou, J. Park, J.-W. Yoo, J.-Q. Wang, J. H. Lee and G. Kim, *ACS Catal.*, 2020, **10**, 4664–4670.
43 L. Wu and J. P. Hofmann, *Curr. Opin. Electrochem.*, 2022, **34**, 101010.
44 M. W. Glasscott, *Curr. Opin. Electrochem.*, 2022, **34**, 100976.

45 R. Jacobs, J. Hwang, Y. Shao-Horn and D. Morgan, *Chem. Mater.*, 2019, **31**, 785–797.
46 C. Wei, Z. Feng, G. G. Scherer, J. Barber, Y. Shao-Horn and Z. J. Xu, *Adv. Mater.*, 2017, **29**, 1606800.
47 G. Kresse and J. Hafner, *Phys. Rev. B: Condens. Matter Mater. Phys.*, 1993, **47**, 558–561.
48 J. Perdew, K. Burke and M. Ernzerhof, *Phys. Rev. Lett.*, 1996, **77**, 3865.
49 J. P. Perdew, A. Ruzsinszky, G. I. Csonka, O. A. Vydrov, G. E. Scuseria, L. A. Constantin, X. Zhou and K. Burke, *Phys. Rev. Lett.*, 2008, **100**, 136406.
50 Y. Sim, J. John, S. Surendran, B. Moon and U. Sim, *Appl. Sci.*, 2018, **9**, 16.
51 S. Ganguli, S. Ghosh, G. Tudu, H. V. S. R. M. Koppisetti and V. Mahalingam, *Inorg. Chem.*, 2021, **60**, 9542–9551.
52 Y. Hou, M. R. Lohe, J. Zhang, S. Liu, X. Zhuang and X. Feng, *Energy Environ. Sci.*, 2016, **9**, 478–483.
53 R. Pohjonen, O. Mustonen, M. Karppinen and J. Lindén, *J. Alloys Compd.*, 2018, **746**, 135–139.
54 C. Simon, M. B. Zakaria, H. Kurz, D. Tetzlaff, A. Blösser, M. Weiss, J. Timm, B. Weber, U. Apfel and R. Marschall, *Chem.–Eur. J.*, 2021, **27**, 16990–17001.
55 J. J. Snyder, T. Caillat and J. P. Fleurial, *Mater. Res. Innovations*, 2001, **5**, 67–73.
56 C. C. L. McCrory, S. Jung, I. M. Ferrer, S. M. Chatman, J. C. Peters and T. F. Jaramillo, *J. Am. Chem. Soc.*, 2015, **137**, 4347–4357.
57 D. R. Brown, T. Day, T. Caillat and G. J. Snyder, *J. Electron. Mater.*, 2013, **42**, 2014–2019.
58 M. Smialkowski, D. Siegmund, K. Stier, L. Hensgen, M. P. Checinski and U.-P. Apfel, *ACS Mater. Au*, 2022, **2**, 474–481.
59 W. Guo, Q. Van Le, H. H. Do, A. Hasani, M. Tekalgne, S.-R. Bae, T. H. Lee, H. W. Jang, S. H. Ahn and S. Y. Kim, *Appl. Sci.*, 2019, **9**, 5035.